RESEARCH ARTICLE

The accuracy of ultrashort echo time MRI sequences for medical additive manufacturing

[1]Maureen van Eijnatten, [2]Erik-Jan Rijkhorst, [2]Mark Hofman, [1]Tymour Forouzanfar and [1]Jan Wolff

[1]Department of Oral and Maxillofacial Surgery/Oral Pathology and 3D InnovationLab, VU University Medical Center, Amsterdam, Netherlands; [2]Department of Physics and Medical Technology, VU University Medical Center, Amsterdam, Netherlands

Objectives: Additively manufactured bone models, implants and drill guides are becoming increasingly popular amongst maxillofacial surgeons and dentists. To date, such constructs are commonly manufactured using CT technology that induces ionizing radiation. Recently, ultrashort echo time (UTE) MRI sequences have been developed that allow radiation-free imaging of facial bones. The aim of the present study was to assess the feasibility of UTE MRI sequences for medical additive manufacturing (AM).
Methods: Three morphologically different dry human mandibles were scanned using a CT and MRI scanner. Additionally, optical scans of all three mandibles were made to acquire a "gold standard". All CT and MRI scans were converted into Standard Tessellation Language (STL) models and geometrically compared with the gold standard. To quantify the accuracy of the AM process, the CT, MRI and gold-standard STL models of one of the mandibles were additively manufactured, optically scanned and compared with the original gold-standard STL model.
Results: Geometric differences between all three CT-derived STL models and the gold standard were <1.0 mm. All three MRI-derived STL models generally presented deviations <1.5 mm in the symphyseal and mandibular area. The AM process introduced minor deviations of <0.5 mm.
Conclusions: This study demonstrates that MRI using UTE sequences is a feasible alternative to CT in generating STL models of the mandible and would therefore be suitable for surgical planning and AM. Further *in vivo* studies are necessary to assess the usability of UTE MRI sequences in clinical settings.
Dentomaxillofacial Radiology (2016) **45**, 20150424. doi: 10.1259/dmfr.20150424

Cite this article as: van Eijnatten M, Rijkhorst E-J, Hofman M, Forouzanfar T, Wolff J. The accuracy of ultrashort echo time MRI sequences for medical additive manufacturing. *Dentomaxillofac Radiol* 2016; **45**: 20150424.

Keywords: magnetic resonance imaging; tomography, X-ray computed; printing, three-dimensional; dimensional measurement accuracy

Introduction

Virtual three-dimensional (3D) surgical planning and additive manufacturing (AM) technologies are increasingly used in oral and maxillofacial surgery. To date, these advanced technologies have proven to be invaluable in dental implant surgery,[1] in the restoration of mandibular fractures,[2] in tumour resections[3] and in maxillofacial reconstructions.[4,5] Moreover, additively manufactured medical constructs such as drill guides,[6] saw guides[7] or individualized implants[8] offer a predictive, functional and aesthetic outcome, especially in patients with anatomical limitations, insufficient mandibular or maxillary bone or poor bone density.[9]

Medical AM comprises three basic steps. The first step is the acquisition of high-resolution medical 3D images that are archived as a digital images and communications in medicine (DICOM) file. The second step is to load the DICOM file into virtual planning software that commonly converts the DICOM file automatically into a virtual 3D surface model in the Standard Tessellation Language (STL) file format.[10] The resulting STL model can then be used to design a medical construct using computer-aided design software. The last step is the conversion of the STL model into a *g*-code that is required to control the AM process.

Currently, 3D medical images intended for oral and maxillofacial AM are acquired using multidetector row CT or CBCT technologies.[11] Both multidetector row CT and CBCT provide high resolution images of the maxillary and mandibular bone and the surrounding tissues.[12] However, the aforementioned technologies have one major disadvantage: they expose the patient to ionizing radiation. The dose levels range between 20 and $400\,\mu Sv$ for CBCT and around $1000\,\mu Sv$ for multidetector row CT modalities, which is about 10–50 times more than a conventional panoramic radiograph (about $20\,\mu Sv$).[13,14] Even though device manufacturers have been developing "ultra" low-dose CT scanning protocols,[15–17] any X-ray-based imaging technology inevitably results in some radiation exposure. Therefore, an alternative, radiation-free imaging modality is still being sought, especially in applications that require a large number of follow-up scans.[18]

Over the past decade, MRI technology has been discussed as an alternative to CT technology for implant planning.[9,19,20] To date, most conventional MRI sequences only offer optimal soft-tissue images and lack the ability to image bone/air interfaces in the head area. This is because MR image acquisition is based on water microenvironments and other sources of protons in the human body. Since the cortical bone has a low proton density and a very short T_2 relaxation time of about 1.5 ms,[21] conventional spin echo and gradient echo MRI sequences are too slow to acquire a sufficient signal from the bone. As a result, new ultrashort echo time (UTE) sequences have been recently developed and successfully used for bone imaging.[22,23] The unique feature of these novel UTE sequences is that they sample the MR signal with a minimum echo time due to radial sampling, and rapidly switch to data recording after the radiofrequency pulse has been delivered.[23]

The MRI of bone using UTE sequences is being applied in several emerging clinical technologies such as positron emission tomography MRI attenuation correction,[22] high-intensity focused ultrasound applications,[24] MR-guided surgery[25] and MR-only treatment planning and guidance in radiotherapy.[26] However, to the best of our knowledge, no studies have been performed on the feasibility of UTE MRI sequences in generating STL models for AM purposes. In this study, we compare the geometric accuracy of UTE MRI-derived STL models of three morphologically different human mandibles with CT-derived STL models. Furthermore, additional geometric inaccuracies introduced during the AM process are assessed.

Methods and materials

Three morphologically different human cadaver mandibles of succumbed Dutch patients with unknown clinical histories and intact bony structures were obtained from the Department of Anatomy, VU University Medical Center, Amsterdam, Netherlands. The mandibles were boiled for 20 h, and all soft tissues were meticulously removed manually.

The outline of this study is summarized in Figure 1. The three dry mandibles were scanned using a CT and a MRI scanner (Step 1). In addition, an optical scan of all three mandibles was acquired using an optical 3D scanner (Artec Spider™; Artec group, Moscow, Russia) with a point accuracy of 0.05 mm. The optical scans of the three mandibles were used as "gold-standard" STL models. The CT and MRI scans were then converted to STL files (Step 2) and aligned with the gold-standard STL models. Subsequently, the geometric deviations between the CT- and MRI-derived STL models and the gold-standard models were calculated. Furthermore, the CT, MRI and gold-standard STL model of one mandible were additively manufactured (Step 3) and scanned again with the optical scanner (Step 4) to map additional geometric deviations introduced during the AM process.

MRI

The mandibular cortical bone has a very short T_2^* of approximately 1.5 ms, and therefore conventional spin or gradient echo sequences are too slow to acquire any bone signal. In UTE imaging, the free induction decay signal is sampled directly with a submillisecond echo time, resulting in a MR signal from the surrounding cortical bone.[22,23]

All three mandibles were scanned using an UTE sequence on a Philips Achieva® 3-T MRI scanner (Philips Healthcare, Best, Netherlands) with an eight-channel head radiofrequency coil using a UTE single-echo sequence. The following scan parameters were used: repetition time = 4.8 ms, echo time$_1$ = 0.14 ms and flip angle = 15°. A non-selective hard radiofrequency pulse was used for excitation, followed by tuning the receive coil. Immediately thereafter, free induction decay sampling was started during ramp-up of the gradients. This procedure resulted in a time between excitation and readout of 0.14 ms. The 3D *k*-space was radially sampled and regridded to a Cartesian co-ordinate system of isotropic $0.5 \times 0.5 \times 0.5$-mm voxels.

CT imaging

CT imaging was performed with a Siemens Somatom® Sensation 64-slice CT scanner (Siemens Medical Solutions, Erlangen, Germany) using a low-dose scanning protocol. The scan parameters were as follows: tube
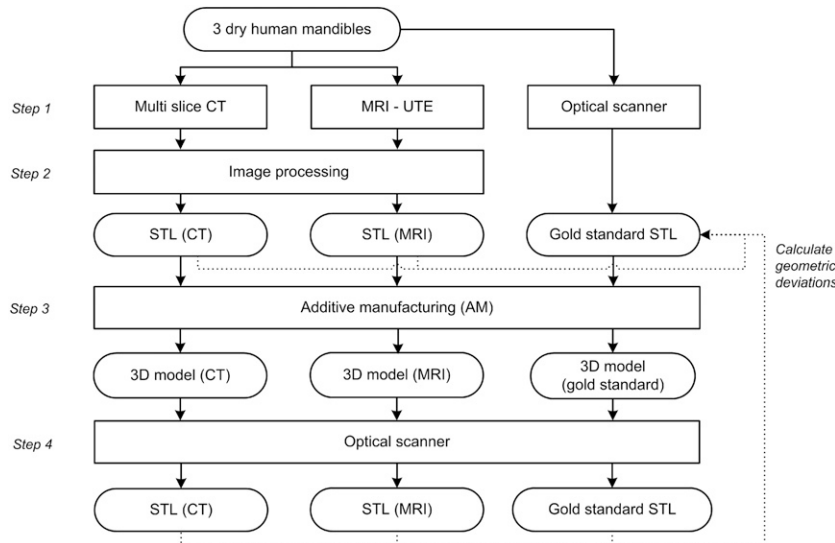
Figure 1 Outline of the study. STL, Standard Tessellation Language; UTE, ultrashort echo time.

voltage = 80 kV, tube current exposure time product = 150 mAs, pixel size = 0.3 × 0.3 mm and slice thickness = 0.6 mm. The images were then reconstructed using a sharp bone convolution kernel (H60h).

Image processing and Standard Tessellation Language deviation analysis
All MRI and CT data sets were saved in DICOM file formats and subjected to the image processing steps described in Figure 2. All CT data sets were imported into Insight Segmentation and Registration Toolkit® software (Kitware Inc., Clifton Park, NY) and manually thresholded using 0 HU. The MRI data sets were thresholded using 15 (Mandibles 1 and 2) and 12 (Mandible 3) arbitrary units (Figure 2, Step 1). These threshold values were chosen just above the MRI background noise signal level to acquire an optimal model of the mandibular bone. Subsequently, all segmented data sets were converted to STL models (Figure 2, Step 2) and imported into MeshLab software (Visual Computing Lab, Pisa, Italy). The MRI- and CT-derived STL models were aligned with their corresponding gold-standard STL models using an iterative closest point algorithm (Figure 2, Step 3). The signed STL-to-STL distances, that is geometric deviations, between all MRI- and CT-derived STL models and the gold-standard STL model were computed using Visualization Toolkit® software (Kitware Inc.) (Figure 2, Step 4) and visualized using colour maps and histograms (Figure 3).

The 95th percentiles of all STL-to-STL distances were calculated using MatLab® software v. 2012 (Math-Works®, Natick, MA). To determine the geometric accuracy in the different areas of interest for surgical planning, the 95th percentiles were calculated for the whole mandible as well as for five different anatomical regions: (1) right ramus with condyle, (2) right body, (3) symphyseal area with alveolar ridge, (4) left body and (5) left ramus with condyle (Table 1).

Additive manufacturing
The CT- and MRI-derived STL models of Mandible 1 were imported into GOM Inspect® software (GOM mbH, Braunschweig, Germany) and smoothed with a surface tolerance of 1.0 mm to correct stair-step artefacts. The smoothed CT-derived STL model, the smoothed MRI-derived STL model and the gold-standard STL model of Mandible 1 obtained using the optical scanner were all printed using a Zprinter 250 inkjet powder printer (3D Systems Inc., Rock Hill, SC). The resulting additively manufactured models were once again scanned with an optical scanner, aligned with the gold-standard STL model and subjected to STL deviation analysis according to Steps 3 and 4 in Figure 2.

Results

All geometric deviations between the optical scan gold-standard STL models and the CT-derived STL models were <1.0 mm (Figure 3a–c), with 95th percentiles <0.5 mm (Table 1), with the exception of Mandible 1 (0.71 mm). The MRI-derived STL models generally presented geometric deviations <2.0 mm (Figure 3d–f), with 95th percentiles <1.5 mm (Table 1), again except for Mandible 1 (1.69 mm).

Figure 4 presents the mean and standard deviation of the signed geometric deviations in the five different anatomical regions of all CT and MRI STL models. The mean value indicates to what extent the STL model was smaller or larger than the gold standard, and the standard deviation indicates the spread in geometric deviations between the STL model and the gold standard. The deviations in all CT-derived STL models were uniformly distributed over the different anatomical regions, whereas all MRI-derived STL models showed a small spread of deviations in the symphyseal area and
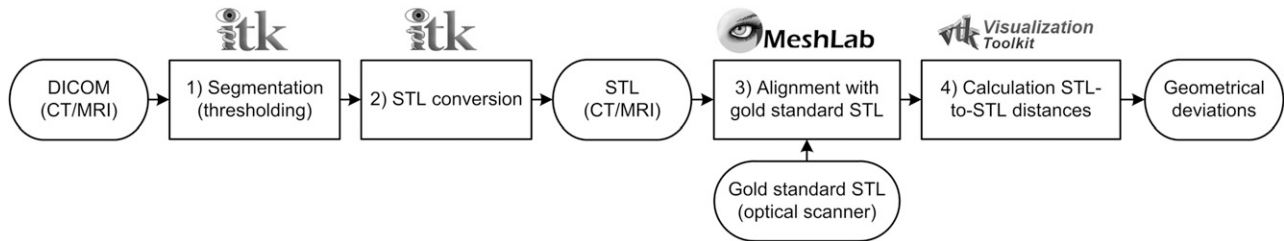
Figure 2 Overview of image processing steps and software packages involved in the Standard Tessellation Language (STL) analysis. The Insight Segmentation and Registration Toolkit® software was obtained from Kitware Inc., Clifton Park, NY, the MeshLab software was obtained from Visual Computing Lab, Pisa, Italy, and the Visualization Toolkit® software from Kitware Inc., Clifton Park, NY. DICOM, digital images and communications in medicine.

a larger spread of deviations in the mandibular condyles (Figure 4).

Minor additional geometric deviations were reported in the additively manufactured 3D models of Mandible 1 (Figure 5). The additively manufactured gold-standard 3D model demonstrated geometric deviations of up to 0.5 mm (Table 2), especially in thin structures such as the coronoid process and alveolar ridge. Geometric deviations in the additively manufactured 3D model obtained using CT data (Figure 5b) were mostly in the vicinity of the coronoid process. In the 3D model

obtained using MRI data (Figure 5c), deviations were observed in the coronoid process, mandibular condyles and alveolar ridge.

Discussion

Today, there is an ever increasing need for high-resolution 3D images for use in surgical planning.[27,28] In this context, CT and CBCT imaging technologies are commonly used and subsequently induce harmful radiation to the
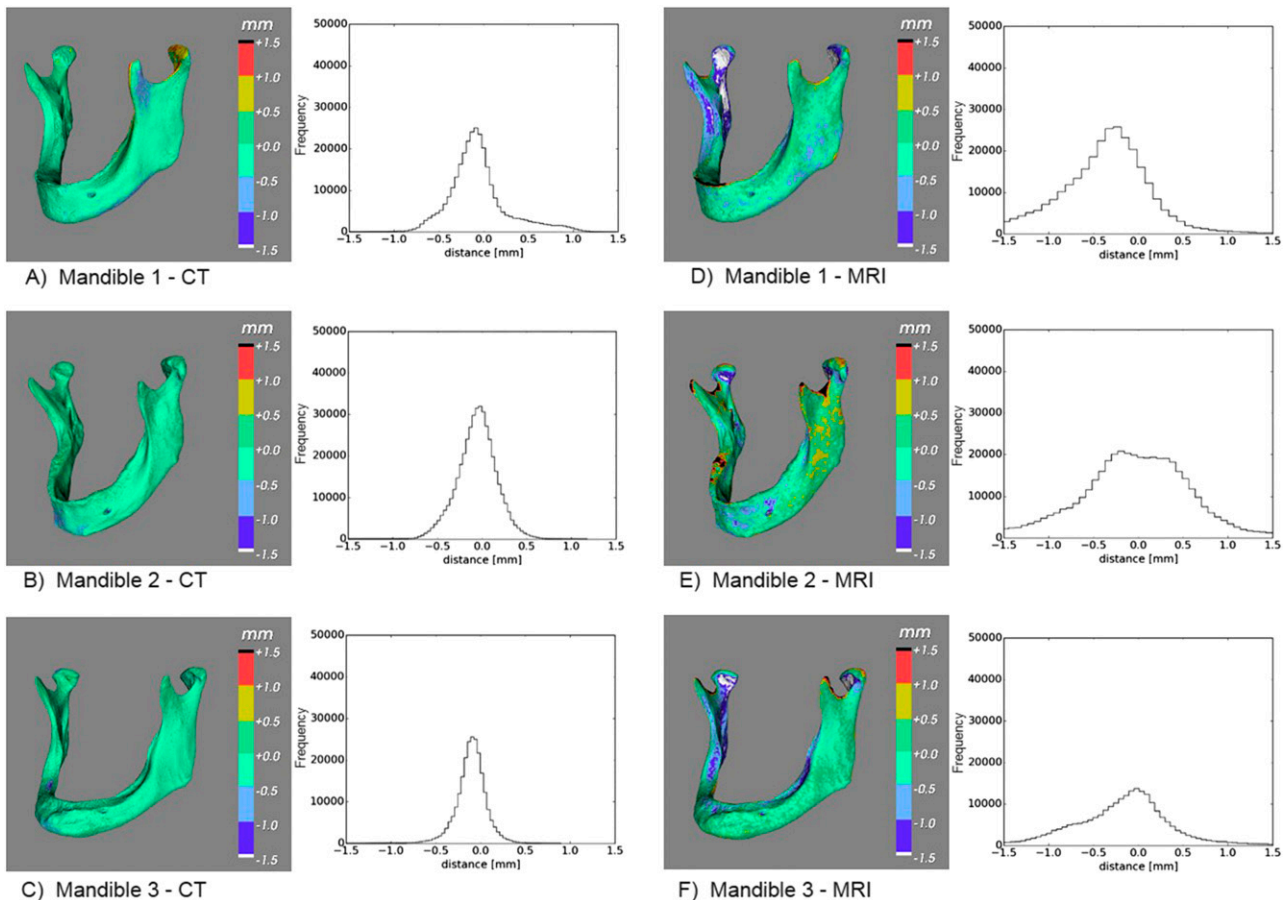

Figure 3 (a–f) Deviations between the CT-derived Standard Tessellation Language (STL) models and the gold-standard STL model (a–c), and the MRI-derived STL models and the gold-standard STL model (d–f), shown in colour maps and histograms.

Table 1 The 95th percentiles of the geometric deviations of five anatomical regions of the mandible in CT- and MRI-derived Standard Tessellation Language models

	CT			MRI		
	Mandible 1 (mm)	Mandible 2 (mm)	Mandible 3 (mm)	Mandible 1 (mm)	Mandible 2 (mm)	Mandible 3 (mm)
Whole mandible	0.71	0.47	0.40	1.69	1.52	1.25
1. Right ramus with condyle	0.49	0.33	0.42	1.89	1.46	1.55
2. Right body	0.30	0.45	0.43	1.03	1.23	0.96
3. Symphyseal area	0.45	0.56	0.45	1.64	0.96	0.70
4. Left body	0.62	0.56	0.30	1.02	1.30	0.86
5. Left ramus with condyle	0.93	0.45	0.34	2.04	1.91	1.53

patient.[29] The cumulative lifetime radiation dose of the population needs to be minimized by reducing the number of overall examinations and the dose resulting from each individual exposure.[30] Hence, radiation-free imaging modalities are still being sought for medical AM.

MR and CT imaging
The novel UTE MRI sequence used in this study produced STL models that were morphologically comparable to those acquired using CT technology (Figure 3). In the MRI-derived STL models, the 95th percentile was generally found to be <1.5 mm (Table 1). The only exception was Mandible 1, which had a 95th percentile of 1.69 mm. These larger geometric deviations were partially due to the submillimetre-thin alveolar ridge of the mandible that could not be imaged due to the limited spatial resolution of the MRI scanner (0.5 mm). Indeed, the 95th percentile of the geometric deviations in the symphyseal area of Mandible 1 was 1.64 mm, compared with 0.96 and 0.70 mm for Mandibles 2 and 3, respectively (Table 1). Another anatomical region that showed slightly larger geometrical deviations in the MRI-derived STL models of all three mandibles were the condyles (Table 1). This phenomenon was most likely caused by a drop in the UTE MRI signal below the chosen threshold value at the edge of the condyles. This lower signal could be due to the higher cortical bone density in the condyle regions. In clinical settings, the presence of soft tissues would offer the possibility to

use more advanced segmentation methods,[22] instead of the thresholding approach used in this study.

In MRI technology, the spatial resolution is dependent on the number of frequency encoding steps and the size of the field of view. Since the size of the mandible determines the minimal field of view, the resolution is dependent on the frequency encoding, that is how often the free induction decay signal is sampled. Therefore, the resolution of the current UTE MRI sequence could be further improved by increasing the duration of the scan; however, this would be a disadvantage in a clinical setting.

In the CT-derived STL models, the 95th percentile of the geometric deviations in the whole mandible was generally found to be <0.5 mm (Table 1). All geometrical deviations were <1.0 mm (Figure 3). The capability of CT to capture small bone structures is also dependent on the spatial resolution of the scanner (0.3 mm), which is directly linked to the hardware properties such as the detector configuration of the scanner.

The aforementioned results are in agreement with a previous study by White et al,[31] who obtained MRI- and CT-derived additively manufactured 3D models of 10 ovine knees, and compared caliper measurements of these models with caliper measurements taken from the real bony anatomy. They reported a mean deviation of 2.15 ± 2.44 mm in their MRI models and a mean deviation of 0.61 ± 0.41 mm in their CT models. Lee et al[32] reported a mean deviation of 0.7 ± 0.1 mm between their MRI-
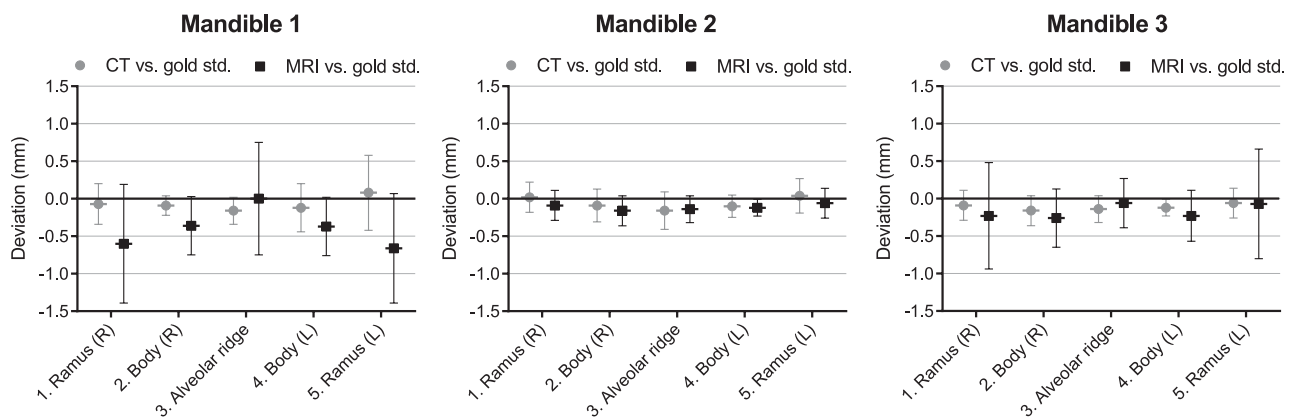

Figure 4 Mean ± standard deviation of the geometric deviations of five anatomical regions of the mandible in CT- and MRI-derived Standard Tessellation Language models. Std., standard.
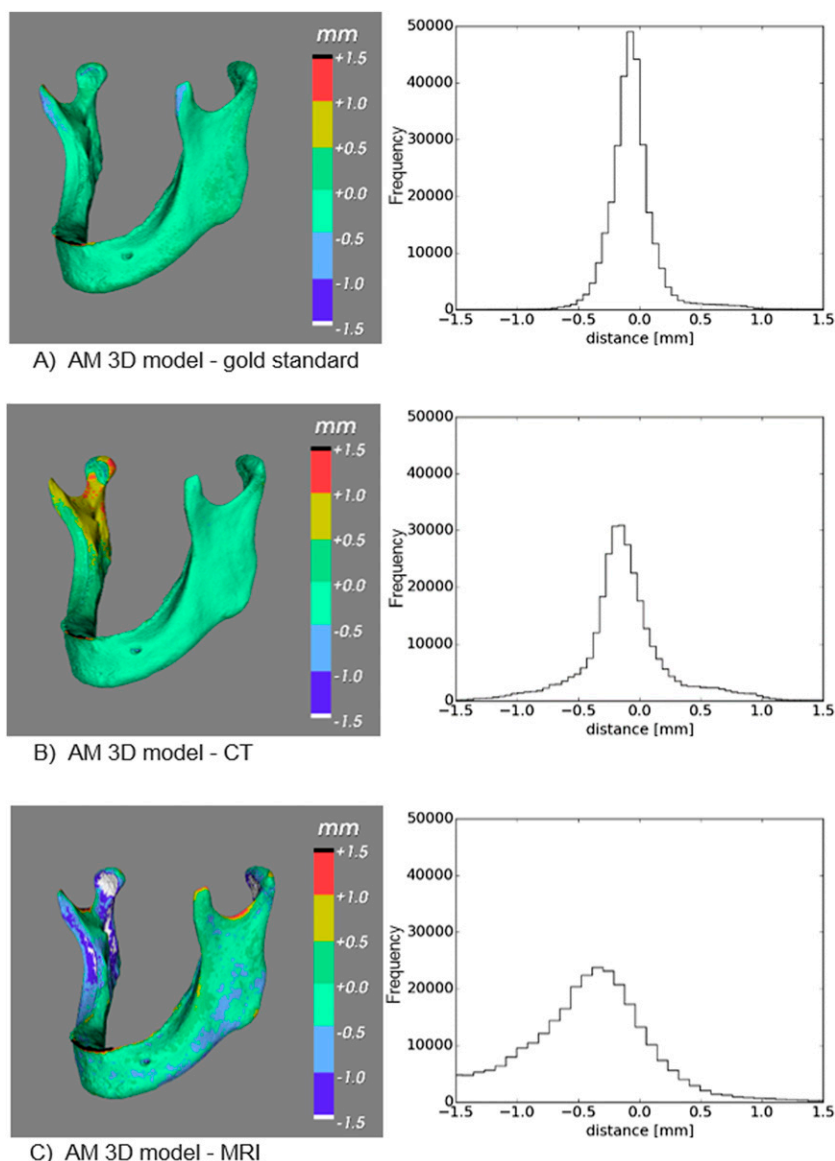
Figure 5 (a–c) Deviations between the additively manufactured (AM) gold-standard three-dimensional (3D) model and the gold-standard Standard Tessellation Language (STL) model; the AM CT-derived 3D model and the gold-standard STL model; and the AM MRI-derived 3D model and the gold-standard STL model shown in colour maps and histograms.

and CT-derived STL models of the femur. A more recent study by Van Den Broeck et al[33] reported root mean square errors of 0.55 mm in their CT-derived STL models of the tibia, and 0.56 mm in their MRI-derived STL models. The results from our study differ from the ones reported by Lee et al[32] and Van Den Broeck et al[33]. This may have been due to differences in the evaluated anatomical structures and the measuring protocols. Moreover, the differences may also have been caused by the different MRI sequences used. White et al,[31] Van Den Broeck et al[33] and Lee et al[32] all used conventional spin or gradient echo sequences that commonly require more manual segmentation of the bone, which in return can be subjective and very time consuming.

The UTE MRI protocol used in this study has certain clinical advantages when compared with CT technologies. The major advantage of MRI is the lack of radiation exposure, which in return allows for multiple imaging sessions to be undertaken. Furthermore, the UTE sequence used in this study combined with other sequences

Table 2 The 50th, 95th and 99th percentiles of the geometric deviations in additively manufactured three-dimensional models of Mandible 1

Percentile	Gold standard (mm)	CT (mm)	MRI (mm)
50th	0.11	0.21	0.48
95th	0.46	0.88	1.73
99th	1.12	1.32	2.63

available on the same MRI device allows for hard and soft tissue visualization, respectively. This can be especially valuable when treating cancer, patients with ameloblastoma and orbital fractures.[34,35]

Additive manufacturing

To quantify the accuracy of the AM process, the gold-standard STL model of Mandible 1 was first additively manufactured and then optically scanned and compared with the original STL model (Figure 5a). The 95th percentile of geometric deviations introduced during the AM process using the gold-standard STL model was 0.46 mm (Table 2). This result suggests that only minor deviations were introduced during the AM process. However, because an optical scanner was used to image the bone, the aforementioned results are not obtainable in clinical settings.

The 95th percentiles of geometric deviations in the MRI- and CT-derived additively manufactured models were higher than those obtained with the optical scanner: 1.73 and 0.88 mm, respectively (Table 2). These results suggest that both CT and MRI have a greater influence on the accuracy of medical AM constructs than the AM process itself.

Limitations of this study

The major limitation of the present study was that mandibles without soft tissues were used. Therefore, the results of this study are not simply generalizable to clinical conditions. In clinical settings, a second UTE MRI echo image is required to discriminate bone from air and soft tissues.[22] Furthermore, motion artefacts due to the relatively long duration of the UTE sequence (several minutes) and metal artefacts caused by orthodontic appliances or fillings can affect the image quality *in vivo*. Further cadaver and patient studies are recommended to assess the feasibility of UTE MRI sequences in clinical settings.

Conclusion

This study demonstrates that MRI of the bone using an UTE sequence is a feasible alternative to CT imaging in the generation of STL models of mandibles with different morphologies and would therefore be suitable for surgical planning and additive AM. The CT and MRI modalities generally introduced geometrical deviations in the STL models of <1.0 and <1.5 mm, respectively. The AM process introduced minor deviations of <0.5 mm. Further *in vivo* studies are necessary to assess the feasibility of the UTE MRI sequence in clinical settings.

References

1. Ramasamy M, Giri, Raja R, Subramonian, Karthik, Narendrakumar R. Implant surgical guides: from the past to the present. *J Pharm Bioallied Sci* 2013; **5**: S98–102. doi: http://dx.doi.org/10.4103/0975-7406.113306
2. Voss JO, Varjas V, Raguse JD, Thieme N, Richards RG, Kamer L. Computed tomography-based virtual fracture reduction techniques in bimandibular fractures. *J Craniomaxillofac Surg* 2016; **44**: 177–85. doi: http://dx.doi.org/10.1016/j.jcms.2015.11.010
3. Yu H, Wang X, Zhang S, Zhang L, Xin P, Shen SG. Navigation-guided en bloc resection and defect reconstruction of craniomaxillary bony tumours. *Int J Oral Maxillofac Surg* 2013; **42**: 1409–13. doi: http://dx.doi.org/10.1016/j.ijom.2013.05.011
4. Schepers RH, Kraeima J, Vissink A, Lahoda LU, Roodenburg JL, Reintsema H, et al. Accuracy of secondary maxillofacial reconstruction with prefabricated fibula grafts using 3D planning and guided reconstruction. *J Craniomaxillofac Surg* Jan 2016. Epub ahead of print. doi: http://dx.doi.org/10.1016/j.jcms.2015.12.008
5. Li Y, Jiang Y, Ye B, Hu J, Chen Q, Zhu S. Treatment of dentofacial deformities secondary to osteochondroma of the mandibular condyle using virtual surgical planning and 3-dimensional printed surgical templates. *J Oral Maxillofac Surg* 2016; **74**: 349–68. doi: http://dx.doi.org/10.1016/j.joms.2015.06.169
6. Dawood A, Marti BM, Sauret-Jackson V, Darwood A. 3D printing in dentistry. *Br Dent J* 2015; **219**: 521–9. doi: http://dx.doi.org/10.1038/sj.bdj.2015.914
7. Mazzoni S, Bianchi A, Schiariti G, Badiali G, Marchetti C. Computer-aided design and computer-aided manufacturing cutting guides and customized titanium plates are useful in upper maxilla waferless repositioning. *J Oral Maxillofac Surg* 2015; **73**: 701–7. doi: http://dx.doi.org/10.1016/j.joms.2014.10.028
8. Kontio R. Update on mandibular reconstruction: computer-aided design, imaging, stem cells and future applications. *Curr Opin Otolaryngol Head Neck Surg* 2014; **22**: 307–15. doi: http://dx.doi.org/10.1097/MOO.0000000000000065
9. Aguiar MF, Marques AP, Carvalho AC, Cavalcanti MG. Accuracy of magnetic resonance imaging compared with computed tomography for implant planning. *Clin Oral Implants Res* 2008; **19**: 362–5. doi: http://dx.doi.org/10.1111/j.1600-0501.2007.01490.x
10. Huotilainen E, Jaanimets R, Valášek J, Marcián P, Salmi M, Tuomi J, et al. Inaccuracies in additive manufactured medical skull models caused by the DICOM to STL conversion process. *J Craniomaxillofac Surg* 2014; **42**: e259–65. doi: http://dx.doi.org/10.1016/j.jcms.2013.10.001
11. Huotilainen E, Paloheimo M, Salmi M, Paloheimo KS, Björkstrand R, Tuomi J, et al. Imaging requirements for medical applications of additive manufacturing. *Acta Radiol* 2014; **55**: 78–85. doi: http://dx.doi.org/10.1177/0284185113494198
12. Rengier F, Mehndiratta A, von Tengg-Kobligk H, Zechmann CM, Unterhinninghofen R, Kauczor HU, et al. 3D printing based on imaging data: review of medical applications. *Int J Comput Assist Radiol Surg* 2010; **5**: 335–41. doi: http://dx.doi.org/10.1007/s11548-010-0476-x
13. Pauwels R, Beinsberger J, Collaert B, Theodorakou C, Rogers J, Walker A, et al. Effective dose range for dental cone beam computed tomography scanners. *Eur J Radiol* 2012; **81**: 267–71. doi: http://dx.doi.org/10.1016/j.ejrad.2010.11.028
14. Lorenzoni DC, Bolognese AM, Garib DG, Guedes FR, Sant'anna EF. Cone-beam computed tomography and radiographs in dentistry: aspects elated to radiation dose. *Int J Dent* 2012; **2012**: 813768. doi: http://dx.doi.org/10.1155/2012/813768
15. Nauer CB, Rieke A, Zubler C, Candreia C, Arnold A, Senn P. Low-dose temporal bone CT in infants and young children: effective dose and image quality. *AJNR Am J Neuroradiol* 2011; **32**: 1375–80. doi: http://dx.doi.org/10.3174/ajnr.A2524
16. Ono K, Hiraoka T, Ono A, Komatsu E, Shigenaga T, Takaki H, et al. Low-dose CT scan screening for lung cancer: comparison of images and radiation doses between low-dose CT and follow-up standard diagnostic CT. *Springerplus* 2013; **2**: 393. doi: http://dx.doi.org/10.1186/2193-1801-2-393
17. Lutz J, Jager V, Hempel MJ, Srivastav S, Reiser M, Jäger L. Delineation of temporal bone anatomy: feasibility of low-dose

64-row CT in regard to image quality. *Eur Radiol* 2007; **17**: 2638–45. doi: http://dx.doi.org/10.1007/s00330-007-0578-1

18. Singh S, Kalra MK, Moore MA, Shailam R, Liu B, Toth TL, et al. Dose reduction and compliance with pediatric CT protocols adapted to patient size, clinical indication, and number of prior studies. *Radiology* 2009; **252**: 200–8. doi: http://dx.doi.org/10.1148/radiol.2521081554

19. Imamura H, Sato H, Matsuura T, Ishikawa M, Zeze R. A comparative study of computed tomography and magnetic resonance imaging for the detection of mandibular canals and cross-sectional areas in diagnosis prior to dental implant treatment. *Clin Implant Dent Relat Res* 2004; **6**: 75–81.

20. Kawai T, Asaumi R, Kagawa T, Inadomi D, Yuasa K, Yosue T. The observation of the incisive branches of mandibular canal—the comparison between MRI *vs*. CBCT. *Clin Oral Implants Res* 2014; **25**: 456. doi: http://dx.doi.org/10.1111/clr.12458_434

21. Horch RA, Nyman JS, Gochberg DF, Dortch RD, Does MD. Characterization of 1H NMR signal in human cortical bone for magnetic resonance imaging. *Magn Reson Med* 2010; **64**: 680–7. doi: http://dx.doi.org/10.1002/mrm.22459

22. Keereman V, Fierens Y, Broux T, De Deene Y, Lonneux M, Vandenberghe S. MRI-based attenuation correction for PET/MRI using ultrashort echo time sequences. *J Nucl Med* 2010; **51**: 812–18. doi: http://dx.doi.org/10.2967/jnumed.109.065425

23. Aitken AP, Giese D, Tsoumpas C, Schleyer P, Kozerke S, Prieto C, et al. Improved UTE-based attenuation correction for cranial PET-MR using dynamic magnetic field monitoring. *Med Phys* 2014; **41**: 012302. doi: http://dx.doi.org/10.1118/1.4837315

24. Huisman M, Lam MK, Bartels LW, Nijenhuis RJ, Moonen CT, Knuttel FM, et al. Feasibility of volumetric MRI-guided high intensity focused ultrasound (MR-HIFU) for painful bone metastases. *J Ther Ultrasound* 2014; **2**: 16. doi: http://dx.doi.org/10.1186/2050-5736-2-16

25. Liao H, Inomata T, Sakuma I, Dohi T. 3-D augmented reality for MRI-guided surgery using integral videography autostereoscopic image overlay. *IEEE Trans Biomed Eng* 2010; **57**: 1476–86. doi: http://dx.doi.org/10.1109/TBME.2010.2040278

26. Metcalfe P, Liney GP, Holloway L, Walker A, Barton M, Delaney GP, et al. The potential for an enhanced role for MRI in radiation-therapy treatment planning. *Technol Cancer Res Treat* 2013; **12**: 429–46.

27. Schendel SA, Jacobson R. Three-dimensional imaging and computer simulation for office-based surgery. *J Oral Maxillofac Surg* 2009; **67**: 2107–14. doi: http://dx.doi.org/10.1016/j.joms.2009.04.111

28. Giannatsis J, Dedoussis V. Additive fabrication technologies applied to medicine and health care: a review. *Int J Adv Manuf Technol* 2009; **40**: 116–27. doi: http://dx.doi.org/10.1007/s00170-007-1308-1

29. Koivisto J. *The use of MOSFET dosimeters and anthropomorphic phantoms in low dose dental CBCT applications*. Helsinki, Finland: University of Helsinki; 2015.

30. *Implications of commission recommendations that doses be kept as low as readily achievable. ICRP publication 22*. Oxford, UK: Pergamon Press; 1973.

31. White D, Chelule KL, Seedhom BB. Accuracy of MRI *vs* CT imaging with particular reference to patient specific templates for total knee replacement surgery. *Int J Med Robot* 2008; **4**: 224–31. doi: http://dx.doi.org/10.1002/rcs.201

32. Lee YS, Seon JK, Shin VI, Kim GH, Jeon M. Anatomical evaluation of CT-MRI combined femoral model. *Biomed Eng Online* 2008; **7**: 6. doi: http://dx.doi.org/10.1186/1475-925X-7-6

33. Van den Broeck J, Vereecke E, Wirix-Speetjens R, Vander Sloten J. Segmentation accuracy of long bones. *Med Eng Phys* 2014; **36**: 949–53. doi: http://dx.doi.org/10.1016/j.medengphy.2014.03.016

34. Apajalahti S, Kelppe J, Kontio R, Hagström J. Imaging characteristics of ameloblastomas and diagnostic value of computed tomography and magnetic resonance imaging in a series of 26 patients. *Oral Surg Oral Med Oral Pathol Oral Radiol* 2015; **120**: e118–30. doi: http://dx.doi.org/10.1016/j.oooo.2015.05.002

35. Schmutz B, Rahmel B, McNamara Z, Coulthard A, Schuetz M, Lynham A. Magnetic resonance imaging: an accurate, radiation-free, alternative to computed tomography for the primary imaging and three-dimensional reconstruction of the bony orbit. *J Oral Maxillofac Surg* 2014; **72**: 611–18.